Journal of The Electrochemical Society, **156** (9) C304-C312 (2009)
0013-4651/2009/156(9)/C304/9/$25.00 © The Electrochemical Society

Enhanced Efficiency of Dye-Sensitized Solar Cells Using Anodic Titanium Oxide Nanotube Arrays

Chien Chon Chen,[a] Wern Dare Jehng,[b] Lu Lin Li,[c] and Eric Wei-Guang Diau[c,z]

[a]*Department of Energy and Resources, National United University, Miaoli 36003, Taiwan*
[b]*Department of Mechanical Engineering, National Chin-Yi University of Technology, Taichung 411, Taiwan*
[c]*Department of Applied Chemistry and Institute of Molecular Science, National Chiao Tung University, Hsinchu 30010, Taiwan*

This paper concerns the microstructure of the anodic titanium oxide (ATO, TiO_2) nanotube (NT) and its use for the dye-sensitized solar cell (DSSC) device. The ATO length was controlled by various electrolytes and anodic time at various constant applied voltages. The lengths of the NTs at 0.3–0.5 and 0.9–22 μm were controlled by 0.5 vol % HF and 0.58 wt % KF aqueous solutions for varied periods of anodization (1–24 h). The 0.5 wt % NH_4F electrolyte in ethylene glycol can produce 4–41 μm for varied periods of anodization (0.5–8 h). ATO made of 0.3 (0.5 vol % HF), 12 (0.5 wt % KF), and 18 μm (0.5 wt % NH_4F) was used for the DSSC anode; the best cell performance attained 0.13, 3.76, and 6.18%. The DSSC made of 18 μm ATO has a short-circuit current density (J_{sc}) of 13.45 mA/cm^2, a fill factor of 0.64, an open voltage (V_{oc}) of 0.72 V, and a photocurrent efficiency of 6.18% under an air mass 1.5 illumination test.
© 2009 The Electrochemical Society. [DOI: 10.1149/1.3153288] All rights reserved.

Manuscript submitted February 9, 2009; revised manuscript received May 18, 2009. Published July 6, 2009.

The ordered nanochannel films with uniform nanopore sizes and tube lengths from 100 nm to 100 μm can be formed on the surfaces of the active metals aluminum,[1] titanium,[2] zinc,[3] tin,[4] and hafnium[5] by the anodization. They hold significant interest owing to their special properties. Nanoporous films have larger surface-to-volume ratios compared with bulk samples. Many studies[6-9] have shown that various properties, such as melting point, optical, electrical, and mechanical behaviors, can be dependent on pore size.

Titania has been used in various applications such as environmental,[10] catalysis,[11] dielectrics,[12] optoelectronics,[13] sensors,[14] and solar cells.[15] Titanium dioxide has three stable phases: anatase, brookite, and rutile.[16] The transformation of those phases depends on the annealing temperature at a constant oxygen pressure, as in an air furnace. In the phases, the rutile TiO_2 is white, and is thermally and chemically a highly stable material, so it is used as a raw material to produce the color white. Because anatase TiO_2 has photoelectric, photocatalyst, and hydrophilic characteristics,[17-20] it is used in solar cells, disinfection, and surface self-cleaning applications. After anodizing the Ti, anodic titanium oxide (ATO) is amorphous, leading to more defects for electron transfers than crystalline TiO_2. Varghese et al.[21] showed that amorphous ATO could be crystallized by heat-treatment. At temperatures between 25 and 230°C, ATO is amorphous; at temperatures between 280 and 450°C, the anatase phase appears; and at temperatures between 480 and 620°C, the rutile phase forms.

In application, the large surface area of the nanoporous TiO_2 film enhances the chemical reaction efficiency. Compact TiO_2 can be easily formed by anodizing or annealing the titanium surface, as is usually done to provide anticorrosion or decorative characteristics. However, an ordered nanotube (NT) array of TiO_2 film cannot be easily formed unless the critical process parameters are controlled. There are two popular methods used to form uniform nanosize TiO_2: Sol–gel and anodization. Gratzel[22] fabricated TiO_2 nanoparticles (NPs) using the sol–gel process for the dye-sensitized solar cell (DSSC) anode. The first ATO NT arrays were formed by Zwilling et al.[23] and were studied in greater detail recently by Beranek et al.,[24] Chu et al.,[25] and Gong et al.,[26] Cai et al.,[27] and Grimes et al..[28] In Ref. [26-28], the TiO_2 NTs were fabricated by anodization, and the various tube lengths could be controlled by the fluoride ions contained in the electrolytes. For example, an aqueous HF-based electrolyte could be grown to a length of 0.5 μm ATO, an aqueous NaF- or KF-based electrolyte to 6.8 μm ATO,[27] and a nonaqueous F ion-based electrolyte to 134 μm ATO.[29]

Mor et al.[30] fabricated the TiO_2 NT using the anodization process for use in the anodes of photocleavage reaction, DSSC, hydrogen sensing, and self-cleaning sensor studies. Peng et al.[31] showed random a TiO_2 NP construct of a porous DSSC electrode with slow electron diffusion. In contrast, an ordered NT structure leads free electrons to a direct pathway to the interface. In the research of Mor et al.,[15] a DSSC anode 0.36 μm long was formed on fluorine-doped tin oxide (FTO) glass, the photocurrent efficiency of which was 2.9% under an air mass (AM) 1.5 solar simulator, and the theoretical ideal photocurrent efficiency is close to 31% for a single photosystem scheme.

Also, Zhu et al.[32] found that the DSSC conversion efficiency was in direct proportion to the TiO_2 length. When TiO_2 NTs were formed on the Ti foil by anodization and the lengths were from 1.9 to 5.7 μm, the photocurrent efficiency was from 1.7 to 3%. According to Smestad et al.,[33] DSSCs made from inexpensive materials are easier to fabricate than an amorphous silicon solar cell. However, the expensive conductive materials (indium tin oxide, ATO, or FTO)[34] raise the cost of DSSC, and a complex process is required to coat TiO_2 particles on the conductive materials. In our work, the DSSC anodes of FTO and TiO_2 particles were replaced with Ti and TiO_2 NTs.

Experimental

ATO fabrication.— The ordered channel array of ATO was fabricated by anodizing titanium (Ti) foil (Aldrich, 99.7% purity). A platinum (Pt) sheet (2 × 2 cm) was used as a cathode during anodization. The distance between the anode and cathode was controlled at 1.5 cm. The ATO NT lengths of 0.3–0.5 and 0.9–22 μm were controlled by 0.5 vol % HF and 0.5 wt % KF aqueous solutions for varied periods of anodization (1–24 h). The 0.5 wt % NH_4F electrolyte in ethylene glycol obtained 4–41 μm ATO lengths for varied periods of anodization (0.5–8 h). The experimental conditions of samples 1–5 are shown in Table I. Sample 1 (0.3–0.5 μm) ATO was grown by a 0.5 vol % hydrogen fluoride (HF, 55 %) + 10 vol % sulfuric acid (H_2SO_4, 98%) solution (pH 1.4) with 20 V applied for 1 h. Samples 2 (1.4–2.7 μm), 3 (0.9–11.5 μm), and 4 (1.0–21.8 μm) were grown by a 0.58 wt % potassium fluoride anhydrous (KF, 99.9%) + 13.8 wt % sodium bisulfate ($NaHSO_4 \cdot 2H_2O$, 99.9%) + 5.9 wt % trisodium citrate dihydrate ($C_6H_5Na_3O_7 \cdot 2H_2O$) solution of pH 4.7, 5.2, and 5.5 with 25 V applied for periods of anodization (1–24 h). Sample 5 (4–41 μm) growth was achieved by the electrolyte (pH 6.8) of 0.5 wt % ammonium fluoride (NH_4F, 99.9%) + 2 wt % H_2O in ethylene glycol [$C_2H_4(OH)_2$] solvent with 60 V applied for periods of anodization (0.5–8 h). After ATO samples were formed by anodization, the samples were then annealed in an air furnace for 450°C for 3 h to form anatase phase ATO. The micromorphology and composition of

[z] E-mail: diau@mail.nctu.edu.tw

Downloaded on 2014-04-25 to IP 140.113.38.11 address. Redistribution subject to ECS terms of use (see ecsdl.org/site/terms_use) unless CC License in place (see abstract).

Table I. The experimental conditions and TiO_2 NT length of samples 1–5.

Sample	Electrolyte type	pH	Applied voltage (V)	Anodization (h)	Length (μm)	Pore size (nm)
1	0.5% HF	1.4	20	1	0.3–0.5	100
2	0.58% KF	4.7	25	1–24	1.4–2.7	80–100
3	0.58% KF	5.2	25	1–24	0.9–11.5	80–100
4	0.58% KF	5.5	25	1–24	1–21.8	80–100
5	0.5% NH_4F	6.8	60	0.5–8	4–41	120 (top), 50 (bottom)

ATO were determined by a scanning electron microscope (JEOL 6500), a transmission electron microscope (JEOL 2100F), and X-ray diffraction (Philips X'Pert Pro).

DSSC packaging and test.— The anatase ATO is then treated with $TiCl_4$ to increase the TiO_2 surface area. According to those tests, the best procedure was to treat $TiCl_4$ twice at 50°C. The TiO_2 electrode was first immersed in a 0.2 M titanium (IV) chloride ($TiCl_4$) solution for 1 h followed by appropriate rinsing and drying (300°C, 30 min); for the second treatment, the films were immersed in $TiCl_{4(aq)}$ (0.1 M, 0.5 h) again and then annealed at either 350 or 450°C for 30 min. To increase the DSSC voltage the films were then coated with a semiconductor of MgO. The sample was immersed in a solution of 0.026 M magnesium oxide (MgO) + 150 mL acetic acid (CH_3COOH) + 100 mL H_2O for 2 min at 50°C, rinsed in ethanol, and annealed in air at 450°C for 1 h again. Finally, the electrode soaked in ethanol containing 5×10^{-4} M $RuL_2(NCS)_2$ (N3 dye) for 7 h to absorb the N3 dye. An FTO glass coated with platinum (Pt) particles by sputtering was used as a counter electrode. The electrolyte containing 0.5 M lithium iodide (LiI) and 0.05 M iodine (I_2) in acetonitrile (CH_3CN, 99.9%) was introduced into the electrodes. To fabricate the NT-DSSC device, we assembled the two electrodes into a sandwich-type cell and sealed it with a hot-melt film (SX1170, Solaronix, 25 μm thickness). A thin layer of the electrolyte was introduced into the space between the two electrodes, and the conducting wires were attached to the DSSC anode and cathode with a silver paste. The photocurrent was produced using an HP model 4140B measuring unit. The N3 dye absorbed on the ATO was measured using UV-visible–near-IR spectrophotometers (Jasco, V-570) at room temperature. The photocurrent conversion efficiency was tested under an AM 1.5 (300 W, 91160-Oriel Solar Simulator, 100 mW cm^{-2}) on a 0.28 cm^2 sample area.

Results and Discussion

ATO processing.— Figure 1 presents sample 1, scanning electron microscopy (SEM) plane and side view of ATO NT arrays on the Ti foil that was anodized in the HF-based electrolyte (pH 1.4). The ordered territory's nanochannel structure has a length of 0.3 μm, pores with a diameter of 100 nm, an interpore distance of 120 nm, a pore wall thickness of 20 nm, a pore density of 8×10^9 pores cm^{-2}, and a porosity of 68.2%. Figures 2-4 show samples 2–4 SEM images of ATO NT arrays on the Ti foil that were anodized in the

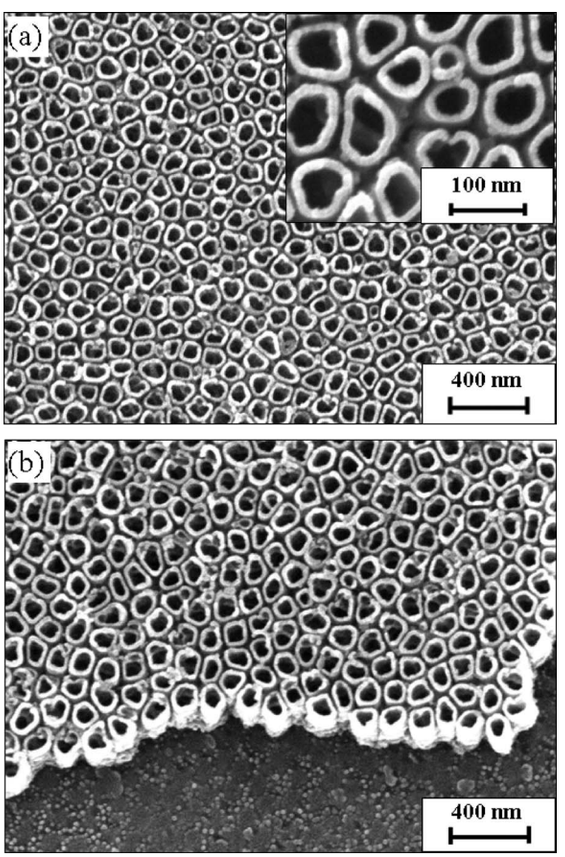

Figure 1. SEM images of the ATO structure formed in 0.5 vol % HF + 10 vol % H_2SO_4 with pH 1.4 solution at 20 V for 1 h. (a) Top view and (b) cross-sectional view of 0.3 μm tube length.

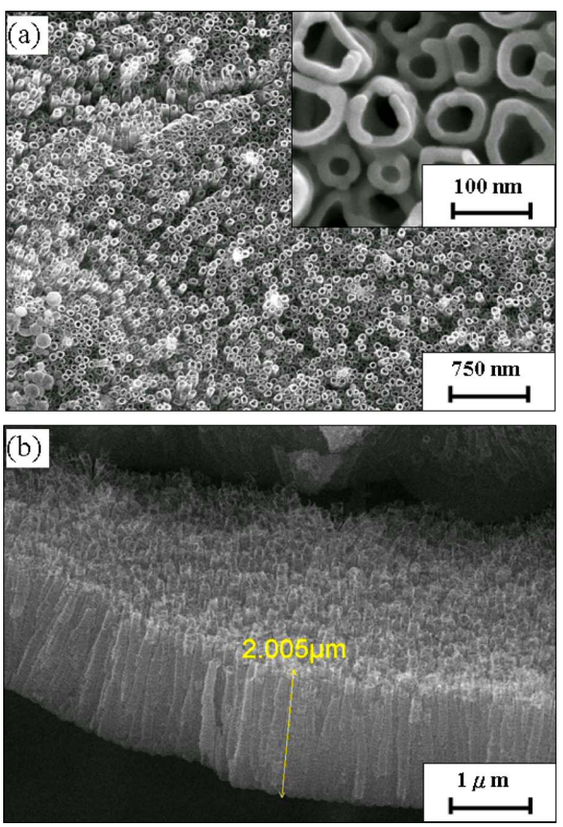

Figure 2. (Color online) SEM images of the ATO structure formed in 0.58 wt % KF + 13.8 wt % $NaHSO_4 \cdot 2H_2O$ + 5.9 wt % $C_6H_5Na_3O_7 \cdot 2H_2O$ with pH 4.7 solution at 25 V for 10 h. (a) Top view and (b) cross-sectional view of 2 μm tube length.

Downloaded on 2014-04-25 to IP 140.113.38.11 address. Redistribution subject to ECS terms of use (see ecsdl.org/site/terms_use) unless CC License in place (see abstract).

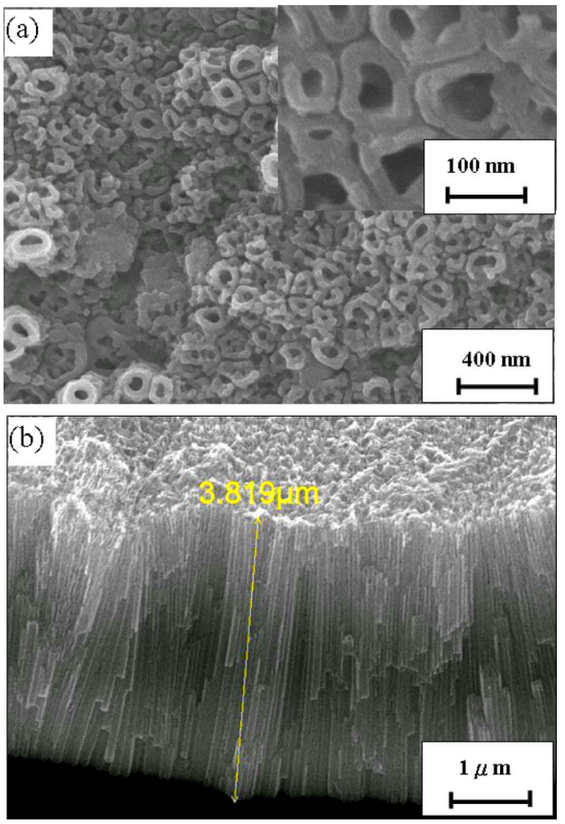

Figure 3. (Color online) SEM images of the ATO structure formed in 0.58 wt % KF + 13.8 wt % $NaHSO_4 \cdot 2H_2O$ + 5.9 wt % $C_6H_5Na_3O_7 \cdot 2H_2O$ with pH 5.2 solution at 25 V for 10 h. (a) Top view and (b) cross-sectional view of 3.8 μm tube length.

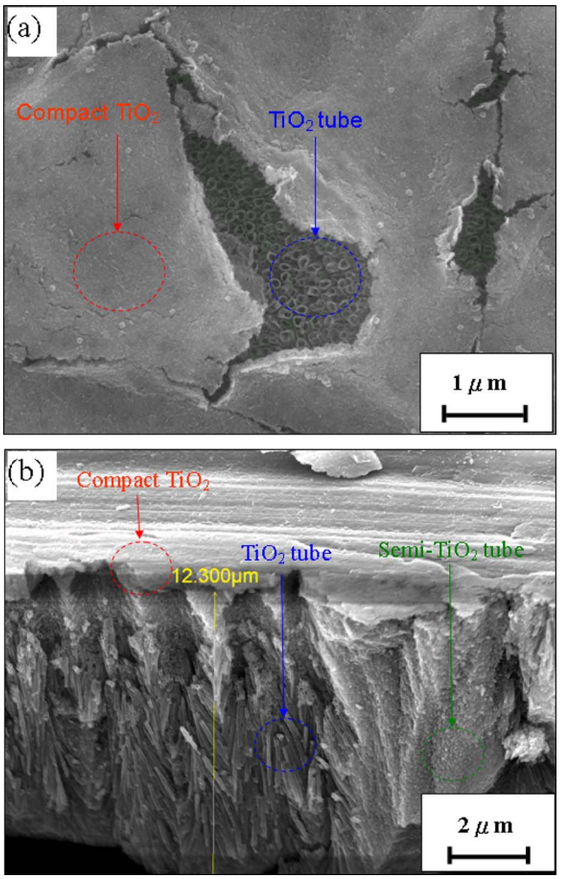

Figure 4. (Color online) SEM images of the ATO structure formed in 0.58 wt % KF + 13.8 wt % $NaHSO_4 \cdot 2H_2O$ + 5.9 wt % $C_6H_5Na_3O_7 \cdot 2H_2O$ with pH 5.5 solution at 25 V for 10 h. (a) Top view and (b) cross-sectional view of 12.3 μm tube length.

KF-based electrolyte (pH 4.7, 5.2, and 5.5). The ATO made by the KF-based electrolyte has a higher pH value than the HF-based electrolyte; therefore, the ATO can grow to several micrometers in length. The images show, the higher the pH value, the thicker the ATO thickness formation, but the more compact film and disorder NT was formed. For example, the pH 5.2 sample has a layer around the NTs, as shown in Fig. 4. In Fig. 5, the ATO structure is not just a NT but a compact film on the surface, and the nanoporous film can be observed in the side view. The unwanted surface deposits on the films introduced during anodization were removed effectively by ultrasonic cleaning in deionized water containing Al_2O_3 as submicrometer particles in a small proportion. After ultrasonic cleaning, a detailed microstructure of the compact film with nanoporous mixed with NTs was present.

A higher anodizing voltage, lower electrolyte temperatures, and lower acid concentrations favor film growth. However, a lower anodizing voltage, higher acid concentrations, and a higher anodizing temperature favor film dissolution. When the rate of film growth has equaled the rate of dissolution of the film in the electrolyte, the thickness of the film remains constant. In our results, samples 2–4 were produced under the same experimental conditions during anodization except for a different pH value of the electrolyte. But, when the electrolyte pH approached acidity the ATO film tended to dissolve in the electrolyte and the shorter ATO film formed. When the electrolyte pH was close to natural, the ATO film tended to grow in the electrolyte and the longer ATO film formed. Figure 6 shows a detail of the sample 3 structure; the (a) SEM and (b) TEM images show the ATO with a ringed structure of the tube. Figure 7 shows the curves of ATO thickness (standing on the Ti substrate) with pH and anodic time (SEM images as shown in the supporting materials). The limited ATO thickness of sample 1 was 0.5 μm after 18 h anodization, and the limited ATO thickness of sample 2 was 3 μm after 18 h anodization. However, the ATO thickness increased with anodized time in the higher pH electrolytes of samples 3–5. In our results, the thicknesses of samples 3 and 4 were 12 and 22 μm, respectively, after 24 h anodization, and sample 5 was 41 μm after 8 h anodization.

Figure 8 shows the SEM images of ATO (pH 6.8) and the side view; the film surface was covered by (a) an unwanted netted film and (b) pores on the top-side tubes, but (c) a continuous bottom tube was observed. Figure 9 shows the SEM images of ATO (pH 6.8); the top view, shows (a) a netted film on the ATO surface. To obtain a clean ATO surface we treated the ATO sample further with ultrasonic vibration for 2–3 min in deionized water. Most of the netted film was removed but the porous tubes are collapsed on (b) the ATO surface that may block the tubes. It is helpful to obtain a (c) clean ATO surface when adding some alumina (Al_2O_3) submicroparticles (average size of 300 nm) in deionized water and the Al_2O_3 particles strike the porous tubes during ultrasonic vibration.

ATO structure.— Figure 11 shows the SEM images of sample 5, a straight NT with hexagonal pore wall and barrier layer structure, and a closed package pore arrangement on the ATO. Because the chemical and electrochemical etching was done on the ATO top and bottom, respectively, during anodization that ATO has a conical column structure of the inner tube. Figure 10a shows a top view of ordering pores with a pore diameter of 120 ± 5 nm, a pore distance of 150 ± 5 nm, and a pore wall thickness of 20 ± 5 nm, and 5

Downloaded on 2014-04-25 to IP 140.113.38.11 address. Redistribution subject to ECS terms of use (see ecsdl.org/site/terms_use) unless CC License in place (see abstract).

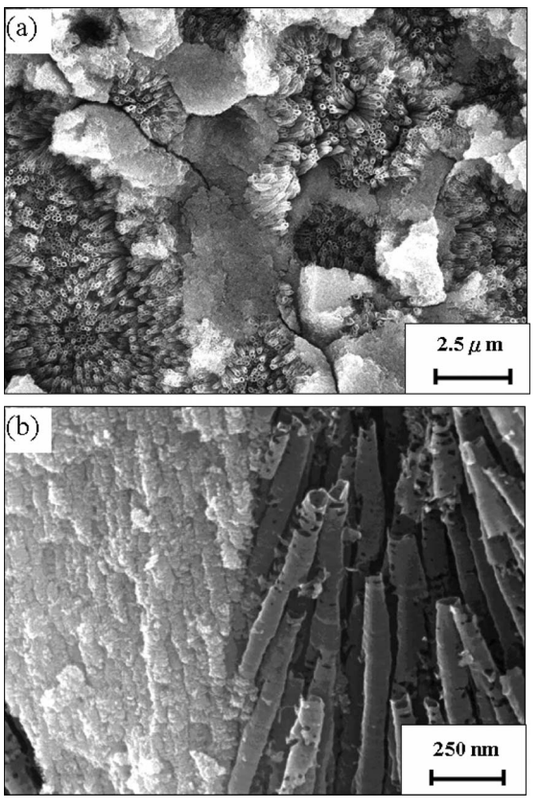

Figure 5. SEM images of pH 5.5 ATO after ultrasonic treatment: The partial formation of a semitube in the ATO. (a) Top view and (b) cross-sectional view.

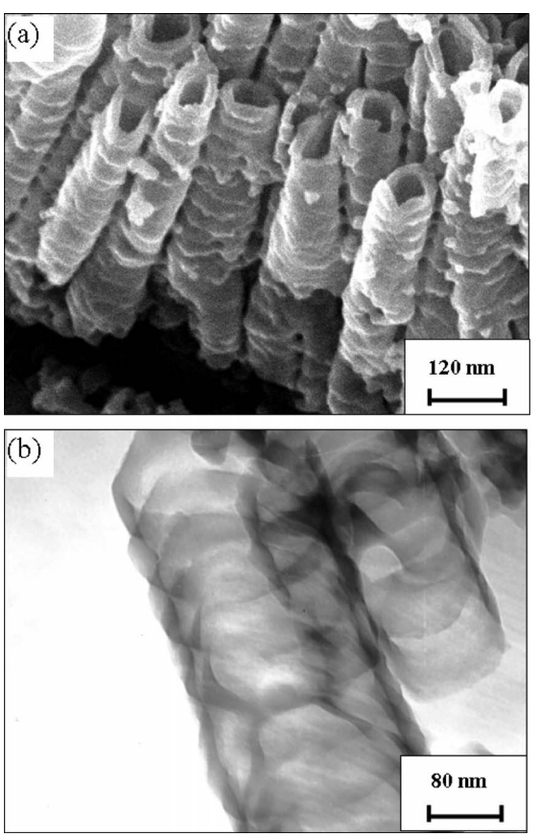

Figure 6. (a) SEM image and (b) TEM image of pH 5.2 ATO with a ringed structure on the tube surface.

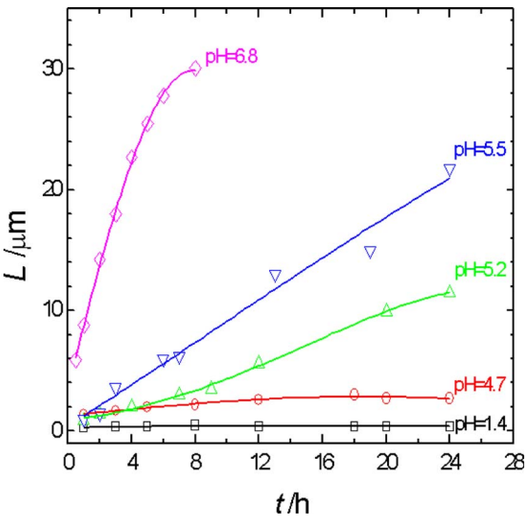

Figure 7. (Color online) Thickness curves of ATO with anodization time when ATO is grown in various pH of electrolytes.

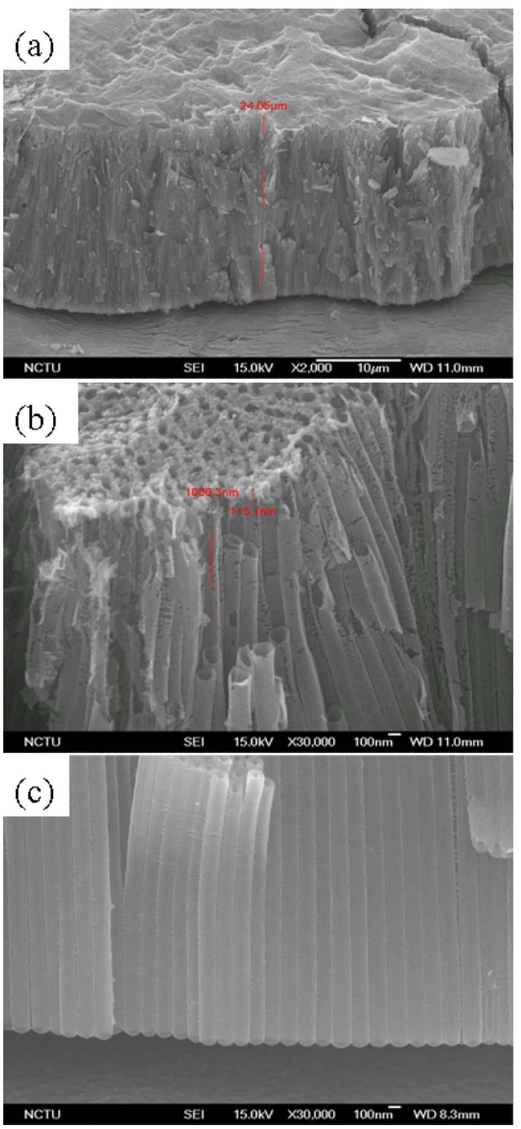

Figure 8. (Color online) SEM images of ATO (pH 6.8), side view: (a) The film surface was covered with an unwanted netted film. (b) Porous structure of the top-side tubes, and (c) continuous structure of the bottom tube.

Downloaded on 2014-04-25 to IP 140.113.38.11 address. Redistribution subject to ECS terms of use (see ecsdl.org/site/terms_use) unless CC License in place (see abstract).

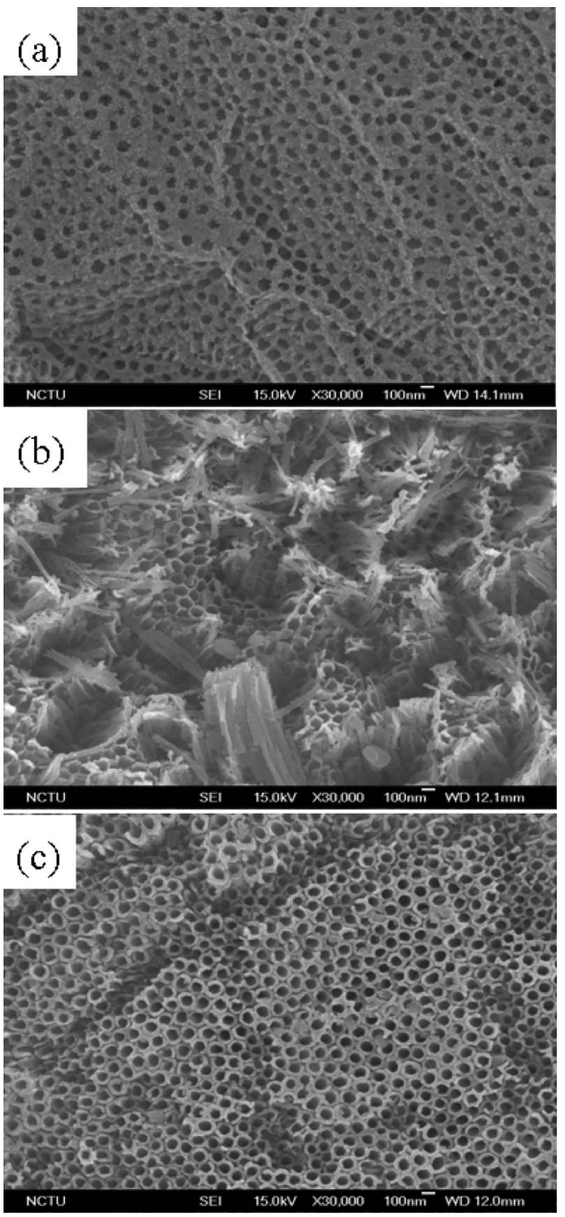

Figure 9. SEM images of ATO (pH 6.8), top view; (a) A netted film on the ATO surface before ultrasonic treatment, (b) porous tubes collapse on the ATO surface after ultrasonic treatment, and (c) a clean ATO surface obtained after ultrasonic treatment with Al_2O_3 particles in deionized water.

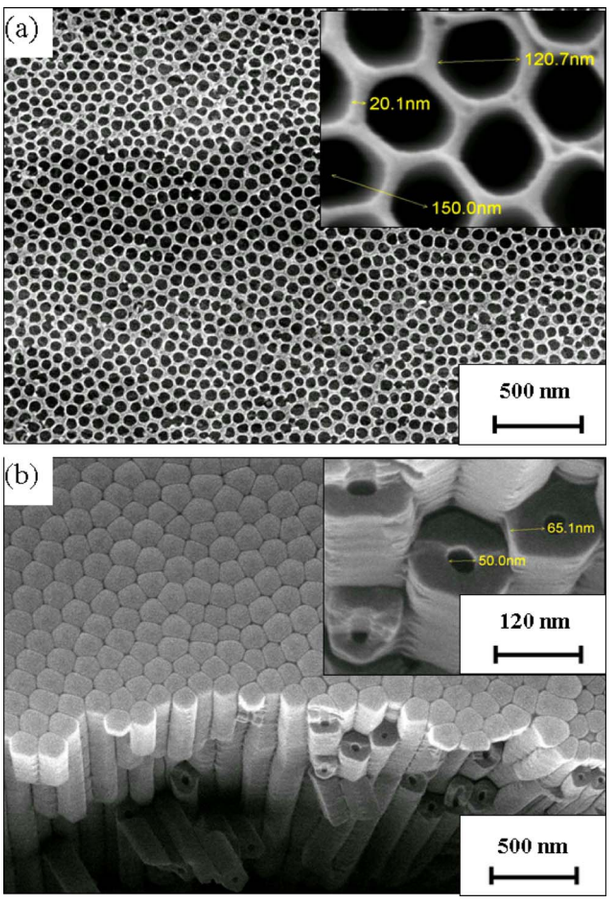

Figure 10. (Color online) SEM images of the ATO structure formed in the 0.5 wt % $NH_4F + C_2H_4(OH)_2$ electrolyte at 60 V for 10 h. (a) Top view: Ordering pores. (b) Bottom view: Compact barrier layer and cross-sectional view of the straight tube.

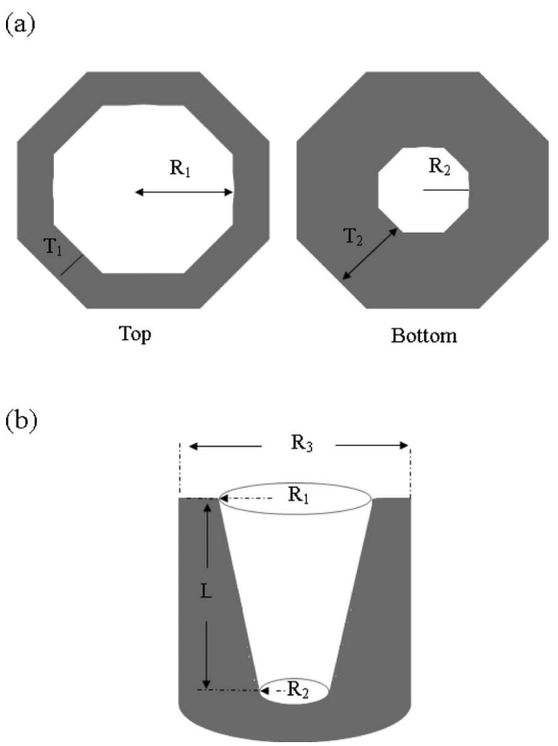

Figure 11. Schematic diagram of the pH 6.8 ATO geometric structure.

$\times 10^9$ pore cm^{-2}. Figure 10b shows a straight tube, of the bottom view, with a compact barrier layer, a bottom pore with a pore diameter of 50 ± 5 nm, a pore wall thickness of 65 ± 5 nm, and an outer column with a diameter of 170 ± 10 nm. Figure 11 is a schematic diagram showing ATO structures wherein the ATO has an open pore on the tube top (Fig. 11a), a closed pore on the bottom part (Fig. 11b), a compact hexagonal column structure of the outer layer, and a hollow conical column structure inside (Fig. 11c). R_1 is the radius of the top pore, t_1 is the pore wall thickness of the top pore, R_2 is the radius of the bottom pore, t_2 is the pore wall thickness of the bottom pore, w is the width of the outer hexagonal layer, and L is the length of the conical column. In Fig. 11c, the volume of the outer compact layer can be expressed as shown in Eq. 1 and the volume of the inner conical form can be expressed as show in Eq. 2

Downloaded on 2014-04-25 to IP 140.113.38.11 address. Redistribution subject to ECS terms of use (see ecsdl.org/site/terms_use) unless CC License in place (see abstract).

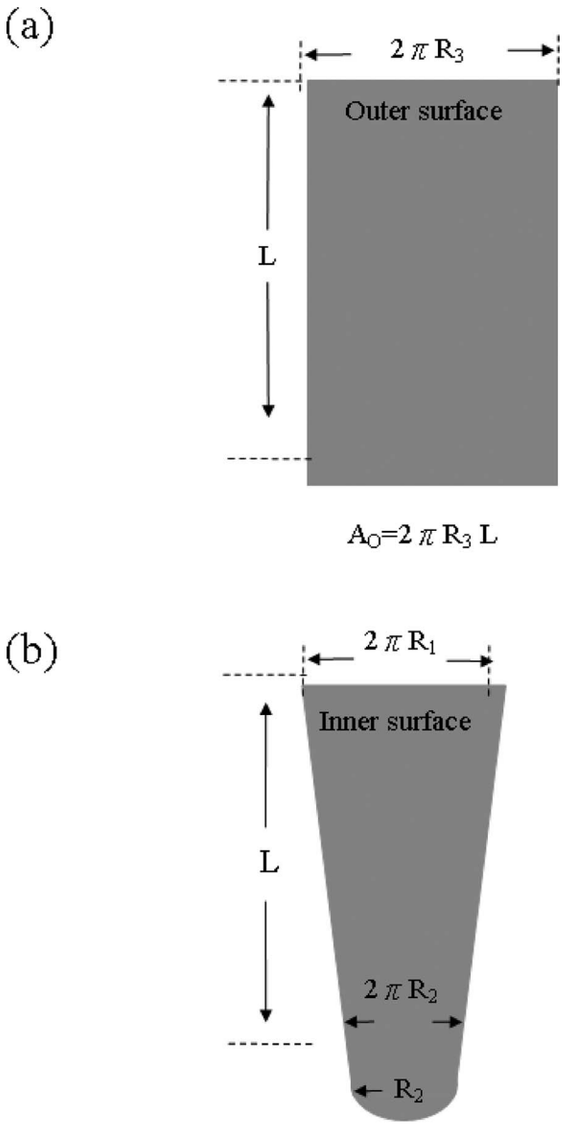

Figure 12. Schematic diagrams of ATO (pH 6.8) enlarged surfaces. (a) The outer ATO surface can be calculated by a rectangular formula. (b) The inner ATO surface can be calculated by trapezoidal and circular formulas.

$$\frac{3}{2}wL(T_1 + R_1) \quad [1]$$

$$\frac{L}{2}(2\pi R_1 + 2\pi R_2) \quad [2]$$

According to Eq. 1 and 2, the porosity of the ATO hexagonal column structure can be evaluated; for example, in our experimental results, w was 40 nm, T_1 was 20 nm, R_1 was 60 nm, T_1 was 20 nm, t was 50 nm, R_2 was 25 nm, and L = 12.95 μm when the ATO porosity was 78.62%. Figure 12 shows the spreading out of ATO. The outer ATO surface area (Fig. 11a) can be calculated by the rectangular formula of Eq. 3, and the inner ATO surface area (Fig. 11a) can be calculated by the trapezoidal and circular formula of Eq. 4

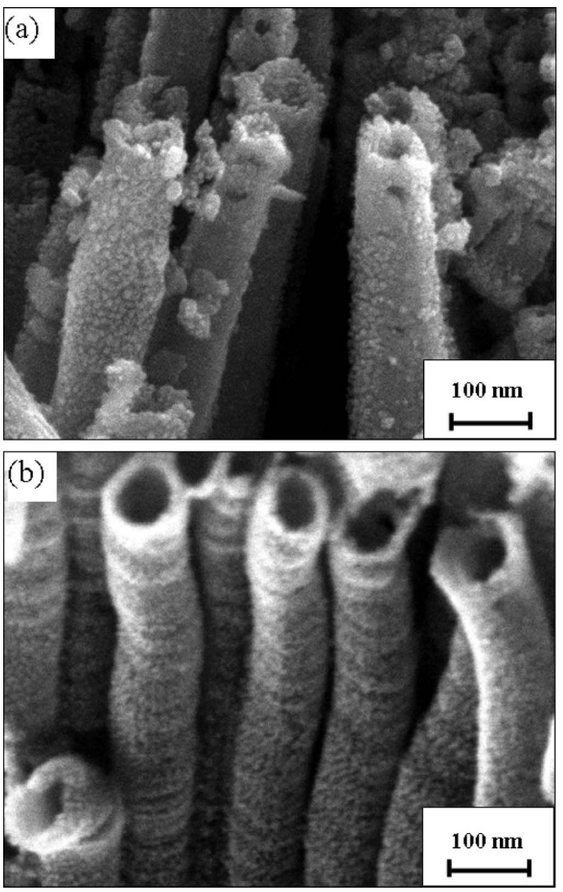

Figure 13. SEM images showed TiO_2 particles on samples 3 and 5 ATO surfaces after $TiCl_4$ treatment.

$$A_O = 2\pi R_3 L \quad [3]$$

$$A_I = \pi(R_1 L + R_2 L + R_2 R_2) \quad [4]$$

Equations 3 and 4 demonstrate that ATO can supply a large adherent surface for sensitized dye. For example, for an ATO sample with a size of 1 cm^2, 8 × 10^9 tube cm^{-2}, and a thickness of 30 μm, the surface area (A_i) is 1790 cm^2. Furthermore, the specific surface area of the film is given by $A = A_i/(V_\rho)$, where ρ is the density of anatase (3.89 g/cm^3) and V is the sample volume, respectively. A specific surface area of 15.34 $m^2\ g^{-1}$ was calculated. Assuming that the TNT layers were comparable to those used in the present work, the surface roughness of the tube walls can be estimated as the ratio of the Brunauer–Emmett–Teller (BET) specific surface area and the calculated specific surface area. This calculation yields a surface roughness factor of around 2.48. According to Lenzmann et al.,[35] a BET study on TiO_2 NT layers treated with $TiCl_4$ gave a calculated surface area of 38 $m^2\ g^{-1}$ which is lower than TiO_2 NP (67.3 $m^2\ g^{-1}$) and TiO_2 nanorod (93.6 $m^2\ g^{-1}$) surface areas.[36] In our present calculations, the ATO without $TiCl_4$ treatment has a calculated surface area of 15.34 $m^2\ g^{-1}$; furthermore, the calculated surface area can be increased to more than two times that of the original.

To increase the TiO_2 NT surface area the ATO can be treated with $TiCl_4$. For example, Fig. 13 shows (a) sample 4 and (b) sample 5 after $TiCl_4$ treatment; a great quantity of TiO_2 NPs formed on the ATO surface and the particle size is under 10 nm. The curves in Fig. 14 show that after $TiCl_4$ treatment (R_1 = 62.5 nm, R_2 = 25 nm, R_3 = 75 nm, R_4 = 1.5 nm, pore density = 8 × 10^9 tube cm^{-2}, and contact angle = 90°) ATO has a larger surface area than before. Fur-

Downloaded on 2014-04-25 to IP 140.113.38.11 address. Redistribution subject to ECS terms of use (see ecsdl.org/site/terms_use) unless CC License in place (see abstract).

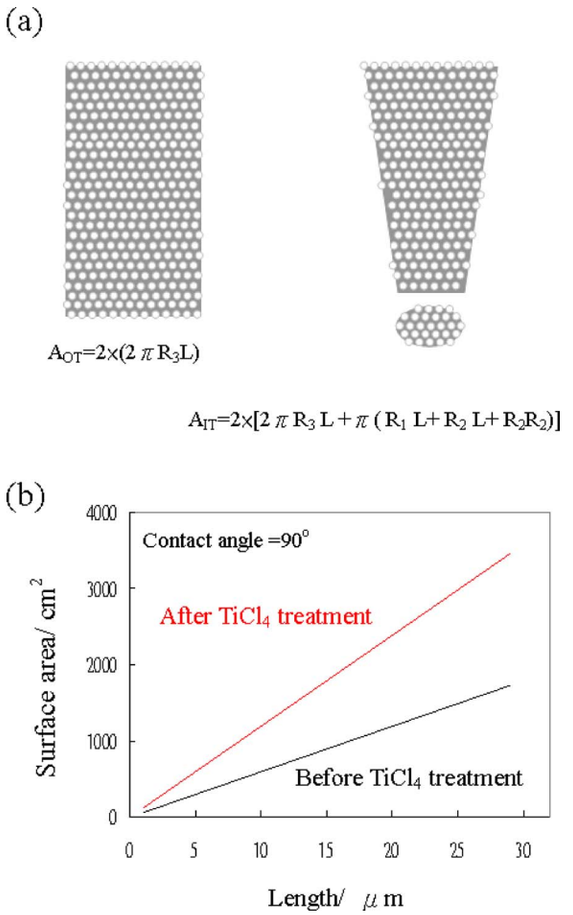

Figure 14. (Color online) The schematic diagram and curve show (a) TiO_2 particles on the ATO inner and outer surfaces and (b) the ATO surface area is doubled after $TiCl_4$ treatment (assuming a TiO_2 contact angle of 90° on the ATO).

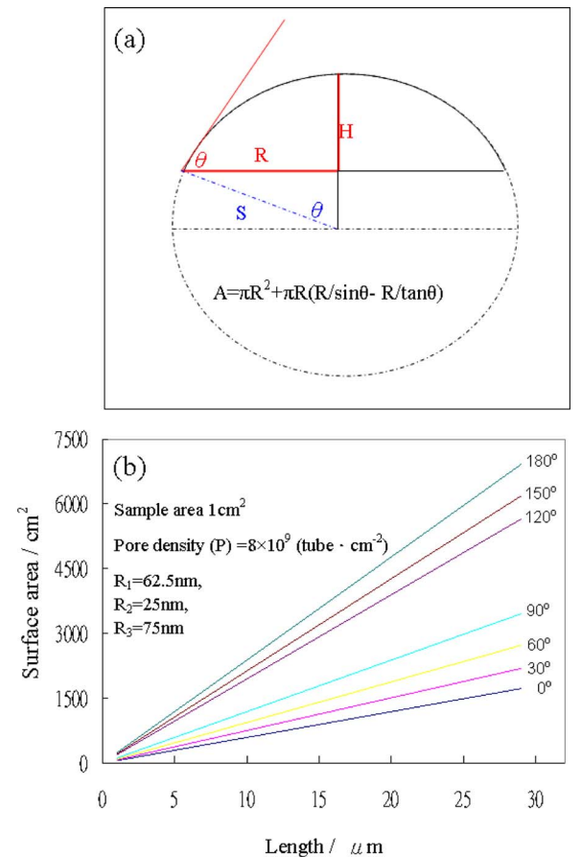

Figure 15. (Color online) The schematic diagram and curve show that (a) the TiO_2 particle surface was dependent on the ATO–TiO_2 contact angle values and (b) the TiO_2 particle surface was proportional to the contact angle value.

thermore, the ATO surface area increased in proportion to the ATO–TiO_2 contact angle. Figure 15a shows a schematic diagram and curve, indicating that (a) the TiO_2 particle surface area was dependent on the ATO–TiO_2 contact angle values and (b) shows that the TiO_2 particle surface was proportional to the contact angle value. From the calculation of Fig. 15a, each TiO_2 particle surface area can be evaluated as Eq. 5 ($\theta \leqq 90°$) and 6 ($\theta = 91–180°$). Figure 15b shows that the TiO_2 particle surface was proportional to the contact angle value. For example, a 30 μm long ATO before $TiCl_4$ treatment (0°) has a surface area of 1970 cm^2 and a specific surface area of 15.34 $m^2\ g^{-1}$. Furthermore, the surface area and specific surface area increase to 4539 cm^2 and 35.34 $m^2\ g^{-1}$, respectively, after $TiCl_4$ treatment (120°)

$$\pi R_4^2 + \pi R_4^2(1/\sin\theta - 1/\tan\theta) \quad [5]$$

$$\pi R_4^2[1/\sin(\theta - 90) - 1/\tan(\theta - 90)] \quad [6]$$

ATO for DSSC application.— The TiO_2 NT has higher electron diffusion lengths (~ 100 μm)[36] which are one dimensional, than the TiO_2 NP. It can be predicted that the DSSC's efficiency can be increased when the TiO_2 NT thickness is increased. However, it has always been a challenge to grow 100 μm TiO_2 NT with good adhesion on the Ti substrate. Our present technology limits the thickness of TiO_2 NT to 20 μm, which has good contact on the Ti substrate.

Because ATO has a larger surface area than the compact TiO_2 film, the N3 dye can be better absorbed on the NT of ATO. Figure 16 shows TEM and energy-dispersive spectroscopy (EDS) mapping images of sample 3 after N3 dye immersion for 8 h. Because N3 dye whose structure has Ru includes the Ru mapping, that N3 dye is absorbed on the TiO_2 tube. To increase the ATO surface to absorb the N3 dye, ATO was given a $TiCl_4$ treatment. Figure 17 shows (a) sample 4 and (b) sample 5 after $TiCl_4$ treatment and then immersion in the N3 dye for 8 h; a great quantity of TiO_2 NPs formed on the ATO surface and the particle size was below 10 nm. Then ATO samples were immersed in the N3 dye for 8 h. Figure 17 and Table II compare the absorbance and photocurrent density–voltage (*J-V*) properties of ATO on the N3 dye and DSSC under simulated AM 1.5 light. In Fig. 17a, except for sample 3, the samples' absorption of the N3 dye increased as the ATO length increased and the absorption spectrum covered most of the visible light region. Sample 3 has a length of 3.5 μm rather than a length of 2.0 μm as for sample 2 but has a more compact layer than sample 2. Therefore, sample 2 displays higher efficiency than sample 3. Even sample 4 has a large compact layer on the surface but the 15 μm still offers 3.76% conversion efficiency. In Fig. 17b the current density is proportional to the ATO length; the 18 μm ATO of sample 5 with 13.45 mA cm^{-2} current density was detected under AM 1.5 light. The photoelectrochemical performance of an ATO anode used in DSSCs is illustrated in Table II; a higher pH of the electrolyte has a longer ATO length and a higher photon-to-current conversion efficiency. Table III shows that sample 5, without $TiCl_4$ treatment, has lower photon-to-current conversion efficiency than that with $TiCl_4$ treatment.

Downloaded on 2014-04-25 to IP 140.113.38.11 address. Redistribution subject to ECS terms of use (see ecsdl.org/site/terms_use) unless CC License in place (see abstract).

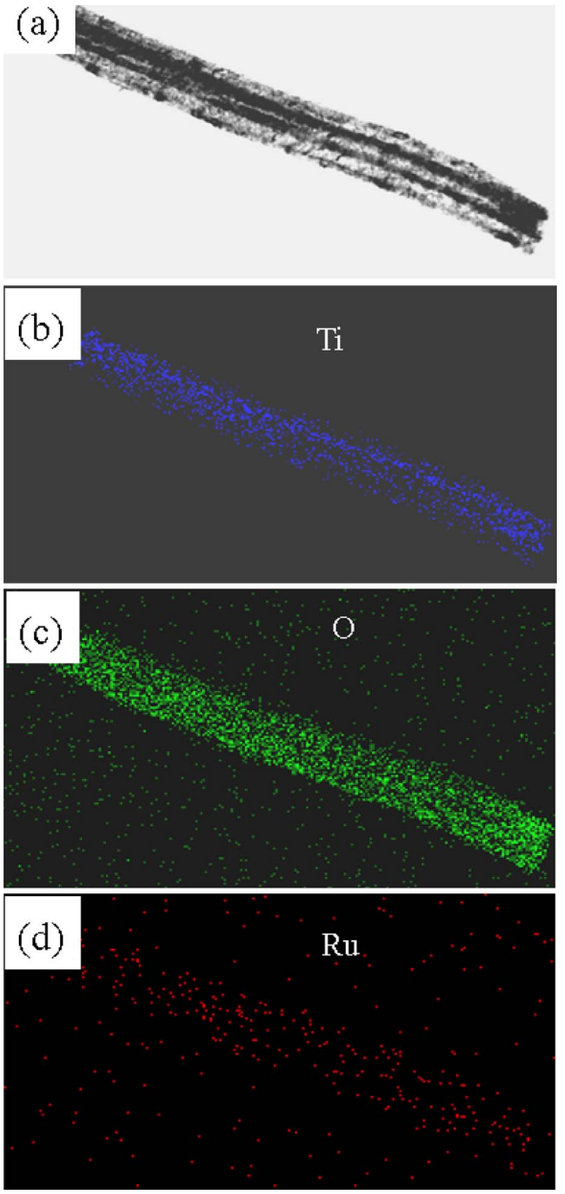

Figure 16. (Color online) TEM and EDS mapping images of the N3 dye with absorbance on the ATO: (a) TEM image, (b) Ti mapping, (c) O mapping, and (d) Ru mapping.

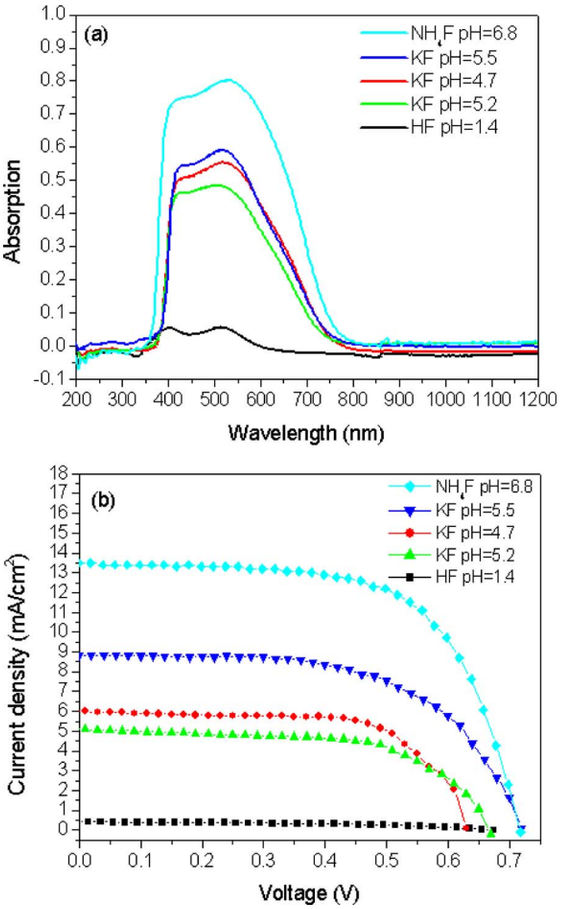

Figure 17. (Color online) ATO samples after N3 dye immersion for 8 h. (a) The absorption spectrum and (b) the *I-V* curve of photocurrent efficiency.

Conclusions

In our study, we presented a simple and inexpensive process for direct formation of ATO on a recyclable material of Ti as a DSSC anode with a large area and a flexible electrode. The ATO size was controllable; the length could be controlled from 0.3 to 41 μm standing on the Ti substrate (with 20 μm, which had good contact on the Ti substrate) depending on the anodic time. After $TiCl_4$ treatment, the ATO surface had TiO_2 particles that increase the ATO surface for N3 dye adhesion. The N3 dye on the ATO could be examined by spectrophotometers or EDS mapping. With this simple process to produce the DSSC anode, the photocurrent conversion efficiency that we attained was 6.18%.

Acknowledgments

National Science Council of Taiwan (contract no. 96-2628-M-009-018-MY2, no. 97-3114-M-009-093, and no. 97-2218-E-239-005) and the MOEATU program provided financial support.

National United University assisted in meeting the publication costs of this article.

Table II. *J-V* characteristics of dye-sensitized TiO_2 NT solar cells after $TiCl_4$ treatment under simulated AM 1.5 light.

Sample	Electrolyte type	L (μm)	J_{sc} (mA cm^{-2})	V_{oc} (V)	FF	η (%)
1	0.5% HF, pH 1.4	0.3	0.42	0.68	0.45	0.13
2	0.58% KF, pH 4.7	2	6.02	0.63	0.67	2.53
3	0.58% KF, pH 5.2	3.5	5.13	0.67	0.62	2.12
4	0.58% KF, pH 5.5	15	8.86	0.72	0.59	3.76
5	0.5% NH_4F, pH 6.8	18	13.45	0.72	0.64	6.18

Downloaded on 2014-04-25 to IP 140.113.38.11 address. Redistribution subject to ECS terms of use (see ecsdl.org/site/terms_use) unless CC License in place (see abstract).

Table III. *J-V* characteristics of sample 5 dye-sensitized TiO_2 NT solar cells without $TiCl_4$ treatment under simulated AM 1.5 light.

Thickness (μm)	J_{sc} (mA cm^{-2})	V_{oc} (V)	FF	Efficiency (%)
6	7.3	0.73	0.61	3.28
13.2	9.04	0.68	0.58	3.41
18	9.06	0.67	0.57	3.47
19.5	9.75	0.65	0.56	3.53

References

1. H. Masuda and M. Yotsuya, *Appl. Phys. Lett.*, **78**, 826 (2001).
2. M. Paulose, H. E. Prakasam, O. K. Varghese, L. Peng, K. C. Popat, G. K. Mor, T. A. Desai, and C. A. Grimes, *J. Phys. Chem. C*, **111**, 14992 (2007).
3. H. Tsuchiya and P. Schmuki, *Electrochem. Commun.*, **6**, 1131 (2004).
4. H. C. Shin, J. Dong, and M. Liu, *Adv. Mater. (Weinheim, Ger.)*, **16**, 237 (2004).
5. H. Tsuchiya and P. Schmuki, *Electrochem. Commun.*, **7**, 49 (2005).
6. K. M. Kulinowski and P. Jiang, *Adv. Mater. (Weinheim, Ger.)*, **12**, 833 (2000).
7. S. H. Tobert, *Phys. Rev. Lett.*, **76**, 4384 (1996).
8. J. Z. Jing and L. Gerward, *J. Appl. Phys.*, **87**, 2658 (2000).
9. S. B. Qadri and J. Yang, *Appl. Phys. Lett.*, **69**, 2205 (1996).
10. X. Quan, S. Yang, X. Ruan, and H. Zhao, *Environ. Sci. Technol.*, **39**, 3770 (2005).
11. Y. Yu, J. C. Yu, Y. Kwok, Y. Che, J. Zhao, L. Ding, W. Ge, and P. Qong, *Appl. Catal., A*, **289**, 189 (2005).
12. N. I. Tatarenko and A. Mozalev, *Solid-State Electron.*, **45**, 1009 (2001).
13. Z. Tun, J. J. Noel, and D. W. Shoesmith, *J. Electrochem. Soc.*, **146**, 988 (1999).
14. O. K. Varghese, G. K. Mor, C. A. Grimes, M. Paulose, and N. Mukherjee, *J. Nanosci. Nanotechnol.*, **4**, 733 (2004).
15. G. K. Mor, K. Shankar, M. Paulose, O. K. Varghese, and C. A. Grimes, *Nano Lett.*, **6**, 215 (2006).
16. M. Pourbaix, *Atlas of Electrochemical Equilibria in Aqueous Solution*, Vol. 213, NACE, Houston, TX, p. 213 (1974).
17. A. Fujishima and K. Honda, *Nature (London)*, **238**, 37 (1972).
18. K. C. Chang, A. Heller, B. Schwartz, S. Menezes, and B. Miller, *Science*, **196**, 1097 (1977).
19. S. Licht and D. Peramunage, *Nature (London)*, **345**, 330 (1990).
20. A. J. Nozik and R. Memming, *J. Phys. Chem.*, **100**, 13061 (1996).
21. O. K. Varghese, D. Gong, M. Paulose, C. A. Grimes, and E. C. Dickey, *J. Mater. Res.*, **18**, 156 (2003).
22. M. Gratzel, *Nature (London)*, **414**, 338 (2001).
23. V. Zwilling, M. Aucouturier, and E. Darque-Ceretti, *Electrochim. Acta*, **45**, 921 (1999).
24. R. Beranek, H. Hildebrand, and P. Schmuki, *Electrochem. Solid-State Lett.*, **6**, B12 (2003).
25. S. Z. Chu, S. Inous, K. Wada, S. Hishite, and K. Kurashima, *Adv. Funct. Mater.*, **15**, 1343 (2005).
26. D. Gong, C. A. Grimes, O. K. Varghese, Z. Chen, W. C. Hu, and E. C. Dickey, *J. Mater. Res.*, **16**, 3331 (2001).
27. Q. Cai, M. Paulose, O. K. Varghese, and C. A. Grimes, *J. Mater. Res.*, **20**, 230 (2005).
28. C. A. Grimes, *J. Mater. Chem.*, **17**, 1451 (2007).
29. M. Paulose, K. Shankar, S. Yoriya, H. E. Prakasam, O. K. Varghese, G. K. Mor, and T. A. Latempa, *J. Phys. Chem. B*, **110**, 16179 (2006).
30. G. K. Mor, O. K. Varghese, M. Paulose, K. Shankar, and C. A. Grimes, *Sol. Energy Mater. Sol. Cells*, **90**, 2011 (2006).
31. T. Peng, A. Hasegawa, J. Qiu, and K. Hirao, *Chem. Mater.*, **15**, 2011 (2003).
32. K. Zhu, N. R. Nwale, A. Miedaner, and A. J. Frank, *Nano Lett.*, **7**, 69 (2007).
33. G. Smestad, C. Bignozzi, and R. Argazzi, *Sol. Energy Mater. Sol. Cells*, **32**, 259 (1994).
34. B. Stjerna, E. Olsson, and C. G. Granqvist, *J. Appl. Phys.*, **76**, 379 (1994).
35. F. Lenzmann, J. Krueger, S. Burnside, K. Brooks, M. Gratzel, D. Gal, S. Ruhle, and D. Cahen, *J. Phys. Chem. B*, **105**, 6347 (2001).
36. J. R. Jennings, A. Ghicov, L. M. Peter, P. Schmuki, and A. B. Walker, *J. Am. Chem. Soc.*, **130**, 13364 (2008).

Downloaded on 2014-04-25 to IP 140.113.38.11 address. Redistribution subject to ECS terms of use (see ecsdl.org/site/terms_use) unless CC License in place (see abstract).